RSC Advances

ROYAL SOCIETY OF CHEMISTRY

www.rsc.org/advances

Discovering P-doped Mechanism in Non-magnetic Ni-P Films for HDD Substrate: A Combined Experimental and Theoretical Study

Guofeng Cui[†]*, Shaofang Liu[†], Kaiming Wang[‡], Qing Li[§], and Gang Wu[§]

[†]Key Laboratory of Low-carbon Chemistry & Energy Conservation of Guangdong Province, School of Chemistry and Chemical Engineering, Sun-Yat Sen University, Guangzhou, 510275, China

[‡] School of Electronic Information and Electrical Engineering, Shanghai Jiao Tong University, Shanghai, 200240, China

[§] Materials Physics and Applications Division, Los Alamos National Laboratory, Los Alamos, New Mexico 87545, United States

Abstract: In this work, a new mechanism is proposed for the redox of hypophosphorous acid catalyzed by a nickel cluster through a combined study of density functional theory (DFT) calculations and electrochemical impedance spectroscopy (EIS) measurements. The DFT results indicate that the concentration of OH^- is a crucial species to control the oxidation and reduction of hypophosphorous acid. The oxidation of hypophosphorous acid preferably takes place at higher OH^- concentration, as OH^- can directly combine with H_3PO_2 and hydrogen radical (H·). In the contrast, reduction is inhibited in this case because the hydrogen radical preferably combines with OH^- rather than H_3PO_2. Thus, pH serves as a key switch to control the pathways of the coupling reaction. EIS results demonstrated that the electroless nickel process includes three electrochemical processes: charge-discharge of electrical double layer, Ni(I) transforming to Ni(II) or Ni(0), and specific adsorption of intermediate products. In good agreement with theoretical prediction, the experimental measurements indicated that an electroless nickel coating with high phosphorous content was successfully synthesized at a low pH, exhibiting non-magnetic properties and enabling its use as a non-magnetic coating for hard disk drive substrates.

Keyword:

Non-magnetic; Phosphorous-doped; Electroless nickel; Mechanism; Hard disk drive (HDD).

1. Introduction

Electroless nickel (EN) deposits have been extensively used in the manufacturing of hard disk drives (HDD) substrates because they are able to exhibit non-magnetic characteristic when phosphorous content is higher than 20.0 at.%.[1] Therefore, it is important to understand how to effectively control the phosphorous content in EN deposits.

The EN process is a complicated heterogeneous catalytic process. It is well known that phosphorous doping in EN is derived from hypophosphite, a reducing agent for EN. During the deposition process, the redox of hypophosphite simultaneously occurs. In particular, the oxidation of hypophosphite leads to the formation of ortho-phosphite. And the reduction of hypophosphite generates phosphorous, resulting in the doping of P into EN deposits. However, to date, the mechanism of the redox coupled reaction has not been fully understood, mainly due to the coupling caused by the shared hypophosphite reactant.

For the oxidation mechanism of hypophosphorous acid, there are two possible reaction pathways. One mechanism was proposed by Van den Meerakker.[2] with hypophosphorous acid release one hydrogen radical directly. The other pathway was proposed by Homma,[3,4] in which hypophosphorous acid should initially combine with one hydroxyl ion. Additionally, Homma calculated the relative energy for all possible intermediates (with DFT on level of MP2/6-311G(d,p)) and the energy barrier of this reaction pathway is 423.4 kJ/mol. However, the transition states and catalytic behavior of nickel species were neglected in the calculations. Compared to the Meerakker's mechanism, the pathway of Homma is more possible according to our previous work.[5] Here, we focus on the Homma pathway to further elucidate the reaction mechanism.

For the reduction mechanism of hypophosphorous acid, there are also two possible reaction mechanisms. One pathway is the direct phosphorous generation mechanism proposed by Brenner.[6] He considered that hypophosphorous acid first loses two hydrogen atoms followed by the breaking of two P-O bonds. The other pathway is an indirect phosphorous generation mechanism proposed by Saitou,[7-9] in which PH_3 is considered to be a key intermediate. In this mechanism, H_3PO_2 firstly breaks two P-O bonds and then one hydrogen radical combines with a phosphorous atom in PH_2 to form PH_3. The two possible mechanisms are evidenced by the electrochemical

measurement data during the electroplating of Ni-P alloy. In this work, we will analyze the feasibility of the double mechanism without considering external electric field.

Many researchers have tried to investigate the mechanisms either by electrochemical[10,11] or quantum chemical modeling methods.[3,4,12,13] However, the results show that a single method cannot fully elucidate the coupled processes. In this work, we explore the double-reaction mechanism through a combination of electrochemical and quantum chemical modeling methods. The results provide new insights on how to control the pathway of the redox reaction of hypophosphorous acid and precisely predict the phosphorous content in the EN deposits.

Furthermore, in order to understand the coupled reaction pathways, the effect of OH^- was investigated. During the EN process, different concentrations of OH^- is found to be able to tune the reduction reaction of hypophosphite, and the OH^- switching mechanism for this coupled reaction is proposed for the first time. The combination of DFT and EIS methods is proved to be an effective way to analyze the mechanism of this complicated electrochemical process.

2. Experimental and calculation Methodology

2.1 EN deposition on Al surface

Aluminum surfaces were polished by SiC with grade 600 and 1200 sandpapers. Then, they were washed with acetone. After the Al samples were rinsed, they were zinc immersion plated. First, the samples were immersed in a solution containing 30 g/L $NiSO_4 \cdot 6H_2O$, 40 g/L $ZnSO_4 \cdot 7H_2O$, 106 g/L NaOH, 10 g/L KCN, 5 g/L $CuSO_4 \cdot 5H_2O$ and 2 g/L $FeCl_3$ at 25±2 °C. After this first zinc immersion, the samples were rinsed by water. Subsequently, the zincate layer was stripped by a 50% nitric acid solution at 25±2 °C for 20-30 s. Then, the samples were rinsed with water. Subsequently, the Al samples were immersed in the zincating immersion solution for a second time. After water rinsing, a uniform and fined zincate film was formed on the Al alloy sample surface.

After the pretreatment, the samples were plated in electroless nickel solution. Electroless nickel solution was prepared with analytical grade reagents and Millipore ultrapure water with a

resistance of 18 MΩ or higher. The solution contained 26 g/L nickel sulfate, 32 g/L sodium hypophosphite, 16 g/L sodium acetate, 4 g/L lactic acid and 8 g/L citrate acid. The electrolytes were heated to 82±1 °C and purged by bubbling N_2 before deposition. The pH value of the electrolyte was adjusted between 4.0 and 9.0 with KOH solution. The pH value was not adjusted again in the measurement process in order to avoid artificial interference. A detailed experimental method is given in our previous work.[14,15]

2.2 Structure and composition analysis

The chemical composition of Ni-P alloys was analyzed by X-ray fluorescence (XRF) spectrometer model S4-Explorer from Brukeraxs (Germany). The XRF spectra were evaluated by the automatic analysis program Spectra plus. Visible reflectance measurements on the EN surfaces were carried out using a 300 mm diameter integrating sphere and a 30 mW He-Ne laser operating at 633 nm. The magnetic properties of samples were analyzed by MPMS XL-7 magnetic property measurement system (Quantum design, Inc.).

2.3 DFT calculation method

All computations reported were carried out with the Gaussian 03 code,[16] employing the hybrid Becke exchange and Lee, Yang, and Parr correlation (B3LYP) [17-19] density functional method. For hydrogen, oxygen, chlorine and phosphorus, 6-311G(d,p) basis sets were used in the present work. The ECP (effective core potential) of the LANL2DZ basis set was adopted by Hay and Wadt for the nickel atoms.[20] Those basis sets are effective on study of the mechanism of electroless[13] and other electrochemical processes.[21,22] Following these works, we have utilized these basis sets in this work. The molecular ground state geometry and vibrational frequency spectra of all species were calculated to determine the reaction pathway potential energy surface. Stationary points were determined with no imaginary components in the vibrational spectra, while transition states were determined with exactly one imaginary vibrational mode. Visual inspection of imaginary vibrational modes was performed with the Gaussian View 3.7 program package.

The solvation effect of an aqueous solution was considered using an explicit solvating model. In the model, the Ni(II) ions complex with two water molecules. Differing from the previous model of Homma, our reaction model is a closed system with hypophosphite ions and Ni(II) ions simultaneously on the nickel cluster surface.

2.4 EIS measurement method

Electrochemical measurements were performed in a three-electrode cell. A 20×50×0.5 mm^3 Al_2O_3 ceramic electrode sputtered by nickel coating was the working electrode. A 10×10×0.3mm^2 platinum foil and a saturated $Hg/HgSO_4$ electrode (MSE) were used as the counter and reference electrodes, respectively. Prior to the measurements, the working electrode was cleaned with ethanol and acetone. The reference electrode was protected by a glass tube filled with saturated K_2SO_4 solution to avoid possible contamination.

EIS was performed on an electrochemical workstation model Ref. 600 (Gamry Inc.). An AC voltage (sinusoidal wave) with amplitude of 10.0 mV was used as the input signal, and the frequency range was set from 10 kHz to 0.5 mHz. A defined sample area of 1.0 cm^2 was exposed to the electrolyte. A Luggin capillary was placed near the working electrode to minimize the ohmic drop. All electrode potentials are referred to saturated $Hg/HgSO_4$ electrode (MSE), if not otherwise stated. All the EIS measurements were performed at the deposition potential E_{dep}, with respect to the MSE reference electrode.

3. Results and Discussion

3.1Effect of phosphorous content on magnetic properties of EN films

The content of phosphorous in EN deposits obtained from different pH solutions is shown in Fig. 1. The incorporated phosphorous content gradually decreases from 13.8 wt% to 4.3 wt%, when pH values are increasing from 5.0 to 9.0. In particular, when the incremental of pH values is 1.0, the corresponding phosphorous mass content decreases *ca.*2.0 percent.

The magnetic properties of EN deposits were measured as a function of phosphorous content of the EN samples (Fig. 2). Obviously, EN5 is magnetic in comparison with the other EN samples in Fig. 2a. The slopes of the line of magnetic force gradually decreased from EN4 to EN1, as shown in Fig. 2b. Additionally, the area of magnetic domain is also reduced as phosphorous content is increased, attributable to a phosphorous interfaced magnetic domain. Furthermore, the structure of the EN film is changed from crystalline to amorphous, when doped phosphorous

content increases. Since the non-magnetic property of the EN coating is essential when it is used as a substrate for HDDs without interference with the magnetic recording material. Thus, EN1with a higher phosphorous content film is more suitable for HDD substrate.

3.2 Coupling reaction pathways from hypophosphorous acid

The coupled reaction pathways for hypophosphorous acid and Ni(II) compounds are illustrated in Scheme 1. The reaction pathways involve one oxidation pathway (OP) and three possible reduction pathways (DRP-I, DRP-II and IRP). As for the OP pathway, the $[Ni\text{-}(H_3PO_2)]^{2+}$ compound first reacts with OH^- to form IM1. Subsequently, the $[Ni\text{-}(H_4PO_3)]^+$ decomposes and releases a hydrogen radical and one electron. This reaction pathway was first proposed by Homma.[13] As for the DRP-I pathway, the $[Ni\text{-}(H_3PO_2)]^{2+}$ compound releases two H· successively. Subsequently, the double bond in P=O turns into a single bond by hydrogenation of the oxygen atom. Finally, the $[Ni\text{-}(H_2PO_2)]^{2+}$ (IM3) compound loses two OH^-. During the DRP-II pathway, a hydrogen intermolecular transferring process occurs from IM1 to IM3 step, differentiating it from the DRP-I pathway. First, the $[Ni\text{-}(H_3PO_2)]^{2+}$ compound releases one hydrogen radical. Next, the P=O double bond is broken *via* hydrogen intermolecular transfer from a phosphorous atom to an oxygen atom. Subsequently, the $[Ni\text{-}(H_2PO_2)]^{2+}$ (IM3) compound releases two OH^- and forms an adsorbed phosphorous atom. In the case of the IRP pathway, the P-O bond breaks before the scission of P-H bonds. The $[Ni\text{-}(H_3PO_2)]^{2+}$ compound (R) turns into $[Ni\text{-}(PH_2)]^{2+}$ (IM3) accompanying with loss of two OH. Subsequently, two hydrogen atoms are released as hydrogen radicals. As a result, the phosphorous atom is doped into the nickel coatings.

3.3 DFT analyze feasibility of reaction pathways

The oxidation pathway and potential energy profile of hypophosphorous acid *via* OP pathway are illustrated in Scheme 1 and Fig. 3, respectively. During the OP pathway, the hypophosphorous acid combines with OH^- and forms IM1 first. In this process, the relative energy of TS1 is 186.5 kJ/mol, which is the highest energy barrier in the whole route. Subsequently, the IM1 compound loses one hydrogen radical and one electron. During the reaction from IM1 to product, the energy barrier is 91.5 kJ/mol. Obviously, the highest energy barrier is the formation of TS1, which is calculated to be 236.9 kJ/mol lower than that in Homma's model.[4] The decreased energy barrier can be attributed to the catalysis of Ni(II) and the Ni_9 cluster.

During the formation of TS1, Ni(II) preferably attracts electron cloud on oxygen in $[Ni\text{-}(H_3PO_2)]^{2+}$. This makes the electropositivity of the phosphorous atom increase in the $[Ni\text{-}(H_3PO_2)]^{2+}$ compound. Additionally, the higher electropositivity of the phosphorous atom is beneficial for combining with OH^-. A detailed charge distribution of IM1 is given in Fig. 7a.

The direct reduction pathway of hypophosphorous acid *via* the DRP-I is illustrated in Scheme 1 and Fig. 4. At first, the P-H bond is broken and the Ni(II) bonds with phosphorous atom at the same time. During the formation of IM1, the energy barrier of TS1 is 42.9 kJ/mol. Then, another P-H bond is broken and the oxygen atom in P=O bond is hydrogenated by a hydrogen radical. Subsequently, the $P\text{-}(OH)_2$ structure is formed as IM3. The calculated highest energy barrier is 132.3 kJ/mol in the DRP-I reaction pathway, associated with the formation of IM3. Finally, the $P\text{-}(OH)_2$ is attacked by hydrogen and forms P and two H_2O by a two-step dehydration reaction.

The direct reduction pathway of hypophosphorous acid *via* the DRP-II pathway is illustrated in Scheme 1 and Fig. 5. Unlike the DRP-I, the P=O bond turns to P-OH *via* hydrogen intermolecular transfer from a phosphorous atom to an oxygen atom. Specifically, the P-H bond is first broken, followed by the hydrogen transfers from phosphorous to oxygen atom resulting in the cleavage of P=O bond. In this process, the calculated energy barrier is 284.6 kJ/mol. Afterwards, the bond of P-OH (IM4) breaks and an adsorbed phosphorous atom is formed.

The indirect reduction reaction pathway *via* the IRP pathway is illustrated in Scheme 1 and Fig. 6. At first, the P=O bond is broken when a hydrogen radical combines with an oxygen atom. In this process, the energy barrier is around 225.9 kJ/mol. These two double P-OH bonds successively break, releasing two hydroxyl radicals. Eventually, the $P\text{-}H_2$ (IM3) breaks and releases two hydrogen radicals. In principle, after overcoming the TS1, the hypophosphorous acid can be rapidly reduced to phosphorous atoms.

Obviously, the energy barrier of the DRP-I pathway is much lower than that of DRP-II and IRP. Thus, the DRP-I pathway is considered to be the dominant reduction pathway for the redox of hypophosphorous acid. At the same time, the energy barrier of IRP is close to that of OP (186.5 vs. 225.9 kJ/mol). As a result, it would be difficult to distinguish these two reactions during electrochemical overpotential measurements.

Fig. 7 shows the critical transition states in the highest barrier site for oxidation and reduction pathways. As for OP-TS1, the highest barrier site in oxidation process is that OH^- combines with hypophosphorous acid. The calculated charges of phosphorous and oxygen atoms are 1.737 and -1.086, respectively. Their charge difference is 2.818, and the barrier of this process is 186.5 kJ/mol.

The (DRP-I)-TS3, (DRP-II)-TS2 and (IRP)-TS1 are the highest barrier sites for reduction pathways. In these three transition states, hydrogen atoms combine with oxygen atoms to break the P=O bond. The charge difference of oxygen in P=O and hydrogen is 1.312, 1.009, 1079 as shown in Fig. 7b, Fig. 7c and Fig. 7d, respectively. In addition, the corresponding energy barriers are 132.3, 284.6 and 225.9 kJ/mol for (DRP-I)-TS3, (DRP-II)-TS2 and (IRP)-TS1, respectively. Thus, the larger charge difference is favorable for reducing the energy barrier during the hydrogenation of P=O process.

3.4 EIS analysis of decomposition of hypophosphorous acid

Fig. 8 reveals the Nyquist impedance spectra of electroless nickel deposition in solution with different pH values. The pH values are increasing from 3.0 to 9.0 with a step of 2.0. In the pH 3.0 solution, there are two typical time constants, corresponding two separate capacitive impedance loops in the high and low frequency domains, respectively. At pH 3.0, the sample cannot be deposited by electroless nickel. With pH increases over pH 5.0, an inductive impedance loop appears in the middle frequency domain and their loops decrease with an increase of pH values in the solution (Fig. 8b). When pH increases from 5.0 to 9.0, the first capacitive impedance loop gradually increases from 4.42 to 8.60 $\Omega\cdot cm^2$ in the high frequency domain.

Fig. 9 shows an equivalent circuit model of $R_s(C_{dl1}R_{t1})(ZR_{t2})(C_{dl2}R_{t3})$ that was used to simulate the EIS spectra. In the equivalent circuit model, R_s represents the resistance of the electrolyte. There is a typical capacitive loop (CL-H) in the high-frequency domain, which is simulated by C_{dl1} and R_{t1} in parallel. There is an inductive loop (IL-M) in the medium-frequency domain, consisting of Z and R_{t2} in parallel. A capacitive loop (CL-L) was also observed in the low-frequency domain, standing for the C_{dl2} and R_{t3} in parallel. Fig. 9b exhibits the comparison of experimental data and simulated results, indicative of a good fitting. The Nyquist plot was obtained at pH 5.8 in the first hour at the deposition potential. Fig. 10 shows the Nyquist

impedance spectra of electroless nickel deposition at different pH values and depositing times. At pH 5.0, there are three time constants observed in the Nyquist plot, including two capacitive loops and one inductance loop. When the pH values increase from 5.0 to 9.0, the diameter of the CL-H loop increases from 5.3 to 25.4 $\Omega\cdot cm^2$ in the high-frequency domain. These results are in agreement with Touhami's research, suggesting the adsorption of hydroxyl species on the electrode surface.[10,11] However, combined with DFT results, the (CL-L) loop corresponds to the Ni-P compound, which closely adsorbs on the Ni surface. At the same time, they are sensitive to hydroxyl, which can combine with a hydrogen radical and lead to the decrease of compound concentration. The result indicates that the doping concentration of phosphorous decreases with an increase of pH. In the meantime, the inductive (IL-M) loop becomes more visible. In addition, the diameter of the CL-L loop increases from 6.5 to 13.2 $\Omega\cdot cm^2$ in the low-frequency domain. Noteworthy, the resistance of three electrochemical processes gradually increase as the depositing time increases, due to the decrease of the reactant concentration (e.g., Ni(II) and $H_2PO_2^-$) and the increase of product concentrations (e.g., $H_3PO_3^-$ and H^+) .

3.5 Catalytic mechanism of hypophosphorous acid

Combining the results of DFT and EIS, the electroless nickel deposition likely proceed through the OP and the DRP-I pathways. They include three typical electrochemical processes, i.e. charge-discharge in electric double layer, adsorption of unstable intermediates on the nickel, and the adsorption of the Ni-P compound intermediates on the nickel. The electrochemical process and relevant species are described in Table 2.

Based on the analysis of DFT, the mechanism for the coupling oxidation and reduction reactions from hypophosphorous acid can be illustrated in Scheme 2. During the electroless nickel deposition process, Ni(II) obtains two electrons and turns to Ni(I) and Ni(0) gradually. The electrons come from the hydrogen radical, when it combines with hydroxyl anion. During the oxidation process of hypophosphorous acid, $[H_3PO_2]$ combines with hydroxyl anion and releases one hydrogen radical. Thus, higher hydroxyl anion concentration is favorable to the oxidation process. On the other hand, during the reduction process of hypophosphorous acid, as $[H_3PO_2]$ releases two hydrogen radical step by step, $[HPO_2]^{2+}$ is able to capture one hydrogen radical and forms $[H_2PO_2]^{2+}$. Then the $[H_2PO_2]^{2+}$ releases two hydroxyl radicals, resulting in the doping of

phosphorous into nickel films. Importantly, reduction process needs one hydrogen radical when hypophosphorous acid switchs to hypophosphate ion. The hydrogen radicals are more stable at a relatively low pH environment, because they tend to combine with hydroxyl anion. Thus, the reduction process will be facilitated in lower hydroxyl anion concentration. Overall, hydroxyl anion is found to be a key species as a switch to control the oxidation and reduction of hypophosphorous acid and a high P content coating is obtained at a low pH solution.

4. Conclusions

This work provide an understand in how to obtain high-phosphorous non-magnetic electroless nickel coatings, which can be applied as hard disk drive surface coatings. During the electroless nickel deposition, the doped phosphorous content increases with decreasing pH values. When pH is lower than 5.0, the coatings start becoming non-magnetic with a phosphorous content over 13.8 wt%. In order to elucidate the phosphorous doping mechanism, the coupled oxidation and reduction reaction pathways of hypophosphorous acid are analyzed by using DFT calculations. The most likely oxidation and reduction reaction pathways are determined to be the OP and DRP-I. Additionally, the electroless nickel process is further illuminated by EIS methods. In particular, there are three electrochemical reaction processes based on the obtained EIS results. The combined EIS and DFT studies can provide new insights into electroless nickel deposition mechanism with controllable phosphorous contents. As a result, a mechanism how the hydroxyl ions inhibit the phosphorous doping during the heterogeneous electrocatalytic process is also discussed.

Author Information

Corresponding Author: Guofeng Cui

*E-mail: cuigf@mail.sysu.edu.cn

Telephone: +86-20-8411-0560

Postal address: Xin Gang Xi Road 135#, School of Chemistry and Chemical Engineering, Sun Yat-Sen University, GuangZhou , 510275, China

Acknowledegments

Dr. G. F. Cui gratefully acknowledges the financial support by National Natural Science Foundation of China (51271205), “the Fundamental Research Funds for the Central Universities” (11lgpy08), “GuangZhou Pearl Technology the Nova Special Project” (2012J2200058), "Research and Application of Key Technologies Oriented the Industrial Development" (90035-3283309, 90035-3283321), “Plan of Science and Technology Project” by DaYa Gulf District in Huizhou City (31000-4207387).

References

1 Z. Qi, and W. Lee, *Tribol. Int.*, 2010, **43**, 810-814.

2 J. E. A. M. Van den Meerakker, *J. Appl. Electrochem.*, 1981, **11**, 395-400.

3 T. Homma, I. Komatsu, A. Tamaki, H. Nakai, and T. Osaka, *Electrochim. Acta*, 2001, **47**, 47-53.

4 H. Nakai, T. Homma, I. Komatsu, and T. Osaka, *J. Phys. Chem. B*, 2001, **105**, 1701-1704.

5 G. Cui, H. Liu, G. Wu, J. Zhao, S. Song, and P. K. Shen, *J. Phys. Chem. C*, 2008, **112**, 4601-4607.

6 A. Brenner, *Electrodeposition of Alloys: Principles and Practice.* Academic Press: New York, 1963.

7 M. Saitou, Y. Okudaira, and W. Oshikawa, *J. Electrochem. Soc.*, 2003, **150**, 140-143.

8 R. L. Zeller III, and U. Landau, *J. Electrochem. Soc.*, 1991, **138**, 1010-1017.

9 T. M. Harris, and Q. D. Dang, *J. Electrochem. Soc.*, 1993, **140**, 81-83.

10 M. E. Touhami, E. Chassaing, and M. Cherkaoui, *Electrochim. Acta*, 2003, **48**, 3651-3658.

11 M. E. Touhami, E. Chassaing, and M. Cherkaoui, *Electrochim. Acta*, 1998, **43**, 1721-1728.

12 T. Homma, A. Tamaki, H. Nakai, and T. Osaka, *J. Electroanal. Chem.*, 2003, **559**, 131-136.

13 T. Homma, H. Nakai, M. Onishi, and T. Osaka, *J. Phys. Chem. B*, 1999, **103**, 1774-1778.

14 G. Cui, N. Li, D. Li, J. Zheng, and Q. Wu, *Surf. Coat. Tech.*, 2006, **200**, 6808-6814.

15 G. Cui, N. Li, D. Li, and M. Chi, *J. Electrochem. Soc.*, 2005, **152**, 669-674.

16 M. J. Frisch, G. W. Trucks, H. B. Schlegel, G. E. Scuseria, M. A. Robb, J. R. Cheeseman, J. A. Montgomery Jr., T. Vreven, K. N. Kudin, J. C. Burant, J. M. Millam, S. S. Iyengar, J. Tomasi, V.

Barone, B. Mennucci, M. Cossi, G. Scalmani, N. Rega, G. A. Petersson, H. Nakatsuji, M. Hada, M. Ehara, K. Toyota, R. Fukuda, J. Hasegawa, M. Ishida, T. Nakajima, Y. Honda, O. Kitao, H. Nakai, M. Klene, X. Li, J. E. Knox, H. P. Hratchian, J. B. Cross, C. Adamo, J. Jaramillo, R. Gomperts, R. E. Stratmann, O. Yazyev, A. J. Austin, R. Cammi, C. Pomelli, J. W. Ochterski, P. Y. Ayala, K. Morokuma, G. A. Voth, P. Salvador, J. J. Dannenberg, V. G. Zakrzewski, S. Dapprich, A. D. Daniels, M. C. Strain, O. Farkas, D. K. Malick, A. D. Rabuck, K. Raghavachari, J. B. Foresman, J. V. Ortiz, Q. Cui, A. G. Baboul, S. Clifford, J. Cioslowski, B. B. Stefanov, G. Liu, A. Liashenko, P. Piskorz, I. Komaromi, R. L. Martin, D. J. Fox, T. Keith, M. A. Al-Laham, C. Y. Peng, A. Nanayakkara, M. Challacombe, P. M. W. Gill, B. Johnson, W. Chen, M. W. Wong, C. Gonzalez, J. A. Pople, *Gaussian 03 Revision C.02,* Gaussian Inc., Pittsburgh PA, 2003.

17 A. D. Becke, *Phys. Rev. A*, 1988, **38**, 3098-3100.

18 A. D. Becke, *J. Chem. Phys.*, 1993, **98**, 5648-5652.

19 C. Lee, W. Yang, and R. G. Parr, *Phys. Rev. B*, 1988, **37**, 785-789.

20 P. J. Hay, and W. R. Wadt, *J. Chem. Phys.*, 1985, **82**, 299-301.

21 E. Jimenez-Izal, F. Chiatti, M. Corno, A. Rimola, and P. Ugliengo, *J. Phys. Chem. C*, 2012, 116, 14561-14567.

22 M. Jafarian, M. Rashvand avei, M. Khakali, F. Gobal, S. Rayati, and M. G. Mahjani, *J. Phys. Chem. C*, 2012, **116**, 18518-18532.

TOC

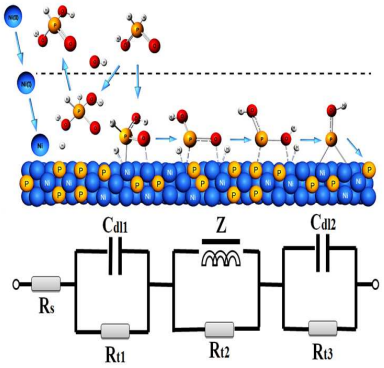

List of tables and figures

Scheme 1. Coupled oxidation and reduction pathways of hypophosphorous acid, including oxidation pathway (OP) shown by black line, direct reduction pathways (DRP-I and DRP-II) shown by red and blue line respectively, and indirect reduction pathway (IRP) shown by green line.

Scheme 2. Coupled oxidation and reduction reaction mechanisms of electroless plating nickel from hypophosphorous acid on nickel surface.

Fig. 1 Phosphorous content (determined by XRF) in EN deposited Ni-P coatings as a function of pH values in solutions ranging from 5.0 to 9.0.

Fig. 2 Magnetic properties of EN deposited Ni-P films (a and b) as a function of phosphorous content, and image of HDD disk obtained with EN1 condition (c).

Table 1. The highest energy barrier of OP, DRP-I, DRP-II and IRP pathways

Fig. 3 Potential energy profile (a) and optimized geometries (b) for oxidation of hypophosphorous acid via the OP pathway. Energy data obtained at B3LYP/6-311G(d,p) level. (Colors: Ni-blue, O-red, P-orange, H-white; Blue arrow-direction of vibration. IM=intermediate, TS=transition state. All energies are relative to the starting materials. The blue arrows represent the vibration mode at the imaginary frequency in the transition state.)

Fig. 4 Potential energy profile (a) and optimized geometries (b) for reduction of hypophosphorous acid via the DRP-I pathway. Energy data obtained at B3LYP/6-311G(d,p) level. (Colors: Ni-blue, O-red, P-orange, H-white; Blue arrow-direction of vibration. IM=intermediate, TS=transition state. All energies are relative to the starting materials. The blue arrows represent the vibration mode at the imaginary frequency in the transition state.)

Fig. 5 Potential energy profile (a) and optimized geometries (b) for reduction of hypophosphorous acid via the DRP-II pathway. Energy data obtained at B3LYP/6-311G(d,p) level. (Colors: Ni-blue, O-red, P-orange, H-white; Blue arrow-direction of vibration. IM=intermediate, TS=transition state. All energies are relative to the starting materials. The blue arrows represent the vibration mode at the imaginary frequency in the transition state.)

Fig. 6 Potential energy profile (a) and optimized geometries (b) for reduction of hypophosphorous acid via the IRP pathway. Energy data obtained at B3LYP/6-311G(d,p) level. (Colors: Ni-blue, O-red, P-orange, H-white; Blue arrow-direction of vibration. IM=intermediate, TS=transition state. All energies are relative to the starting materials. The blue arrows represent the vibration mode at the imaginary frequency in the transition state.)

Fig. 7 NBO charge distribution of TS1, TS3, TS2 and TS1 in the highest barrier site for OP, DRP-I, DRP-II and IRP pathways including Ni_9 clusters and Ni(II) ions. The data is obtained at the B3LYP/6-311G(d,p) level for main group element atoms and at the LANL2DZ level for Ni. (Colors: Ni-blue, O-red, P-orange, H-white, Cl-green; Orange arrow-direction of vibration.)

Fig. 8 Nyquist impedance spectra of EN deposition in solutions with pH values of 3.0, 5.0, 7.0 and 9.0 (a), and partial spectra magnified image (b).

Fig. 9 An equivalent circuit model (a), and the simulated and measured impendent spectra from a solution with pH 5.8 bath in the first hour for EN process (b).

Fig. 10 Nyquist plots of electroless nickel deposition in solutions with pH values of 5.0 (a), 7.0 (b) and 9.0 (c) at different reaction times.

Table 2. Relationship of Nyqiust plot and interface reaction characteristic

Tables and Figures

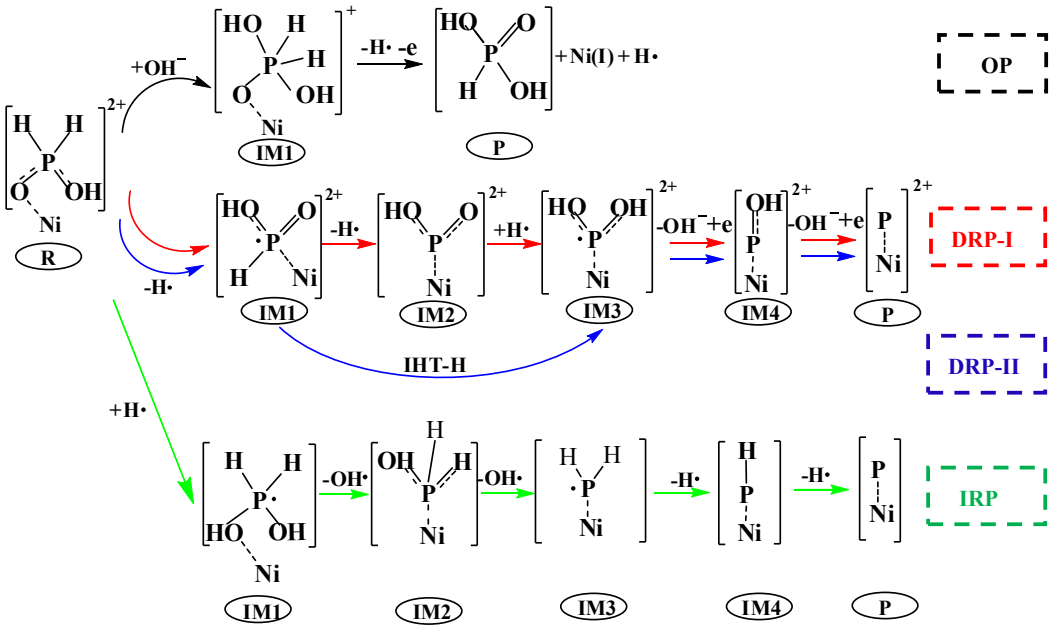

Scheme 1. Coupled oxidation and reduction pathways of hypophosphorous acid, including oxidation pathway (OP) shown by black line, direct reduction pathways (DRP-I and DRP-II) shown by red and blue line respectively, and indirect reduction pathway (IRP) shown by green line.

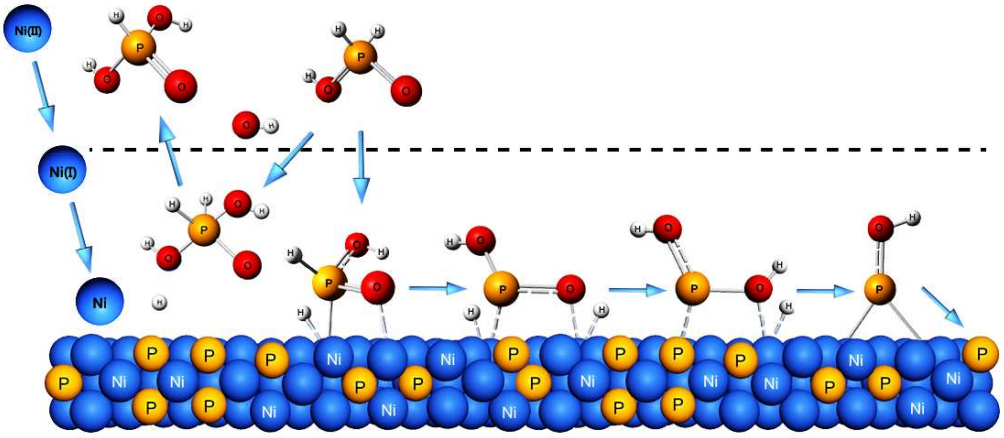

Scheme 2. Coupled oxidation and reduction reaction mechanisms of electroless plating nickel from hypophosphorous acid on nickel surface.

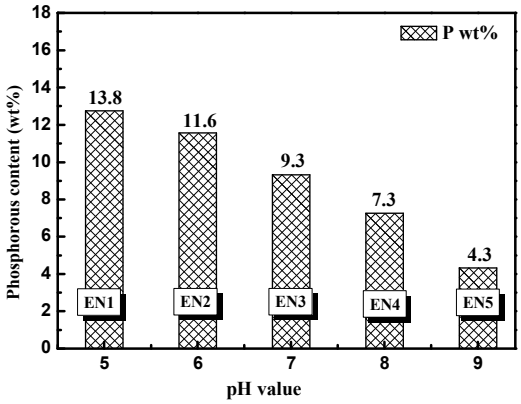

Fig. 1 Phosphorous content (determined by XRF) in EN deposited Ni-P coatings as a function of pH values in solutions ranging from 5.0 to 9.0.

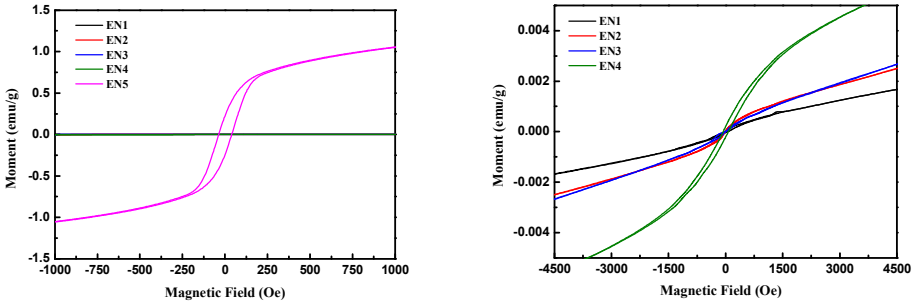

(a) (b)

(c)

Fig. 2 Magnetic properties of EN deposited Ni-P films (a and b) as a function of phosphorous content, and image of HDD disk obtained with EN1 condition (c).

Table 1. The highest energy barrier of OP, DRP-I, DRP-II and IRP pathways

Pathways	OP	DRP-I	DRP-II	IRP
The highest energy barrier(kJ/mol)	186.5	132.3	284.6	225.9

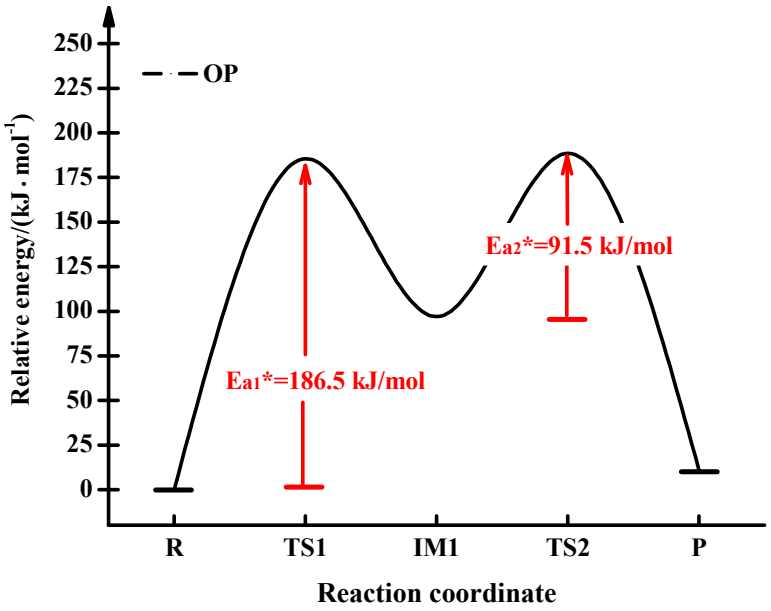

(a)

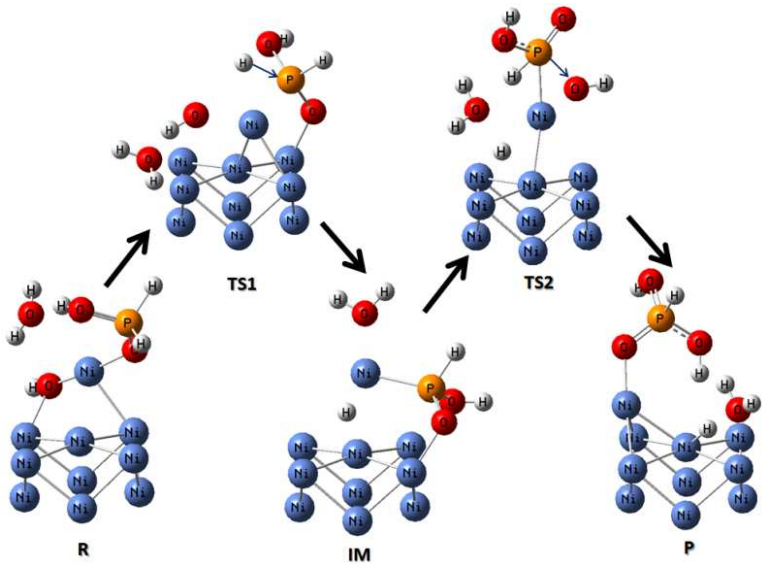

(b)

Fig. 3 Potential energy profile (a) and optimized geometries (b) for oxidation of hypophosphorous acid via the OP pathway. Energy data obtained at B3LYP/6-311G(d,p) level. (Colors: Ni-blue, O-red, P-orange, H-white; Blue arrow-direction of vibration. IM=intermediate, TS=transition state. All energies are relative to the starting materials. The blue arrows represent the vibration mode at the imaginary frequency in the transition state.)

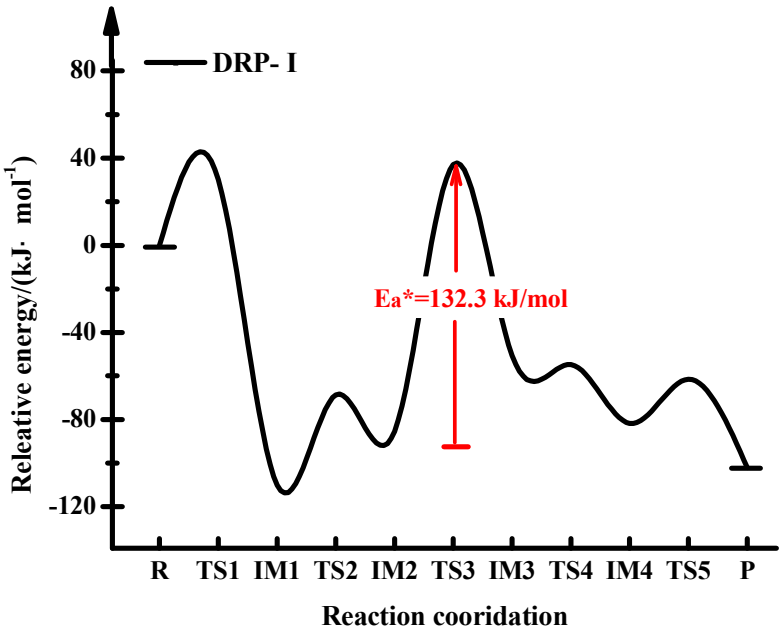

(a)

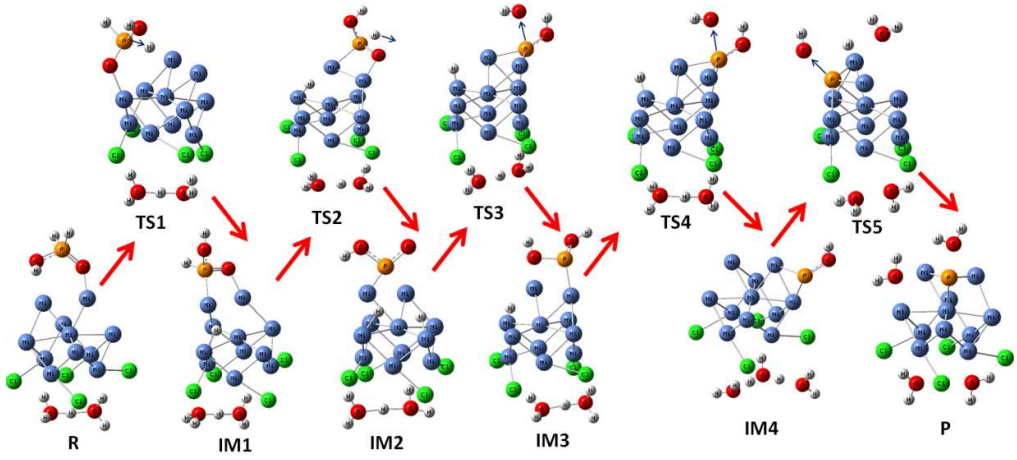

(b)

Fig. 4 Potential energy profile (a) and optimized geometries (b) for reduction of hypophosphorous acid via the DRP-I pathway. Energy data obtained at B3LYP/6-311G(d,p) level. (Colors: Ni-blue, O-red, P-orange, H-white; Blue arrow-direction of vibration. IM=intermediate, TS=transition state. All energies are relative to the starting materials. The blue arrows represent the vibration mode at the imaginary frequency in the transition state.)

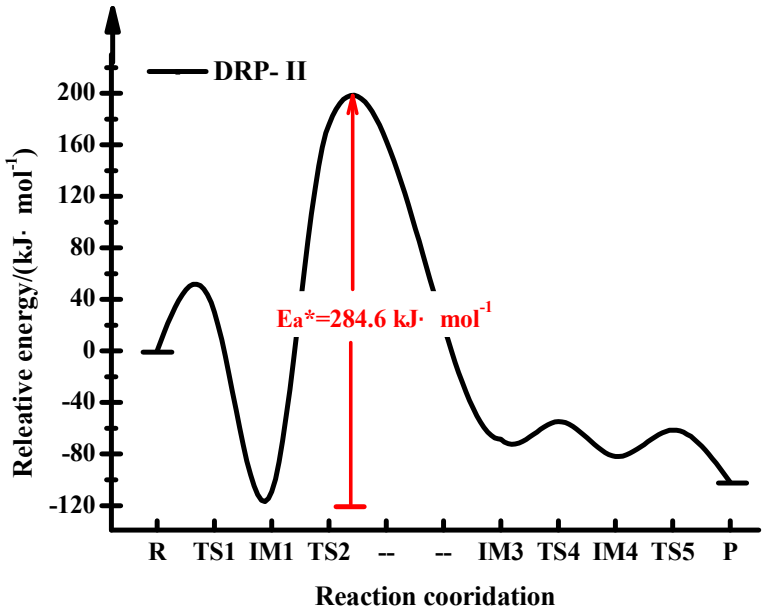

(a)

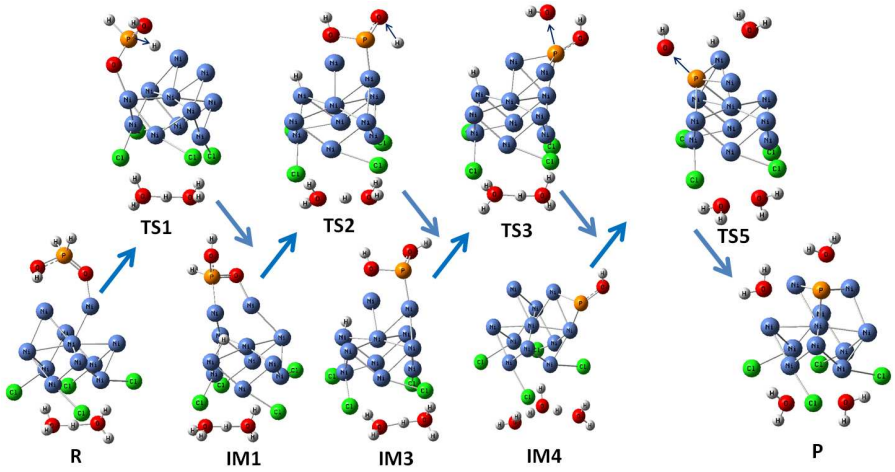

(b)

Fig. 5 Potential energy profile (a) and optimized geometries (b) for reduction of hypophosphorous acid via the DRP-II pathway. Energy data obtained at B3LYP/6-311G(d,p) level. (Colors: Ni-blue, O-red, P-orange, H-white; Blue arrow-direction of vibration. IM=intermediate, TS=transition state. All energies are relative to the starting materials. The blue arrows represent the vibration mode at the imaginary frequency in the transition state.)

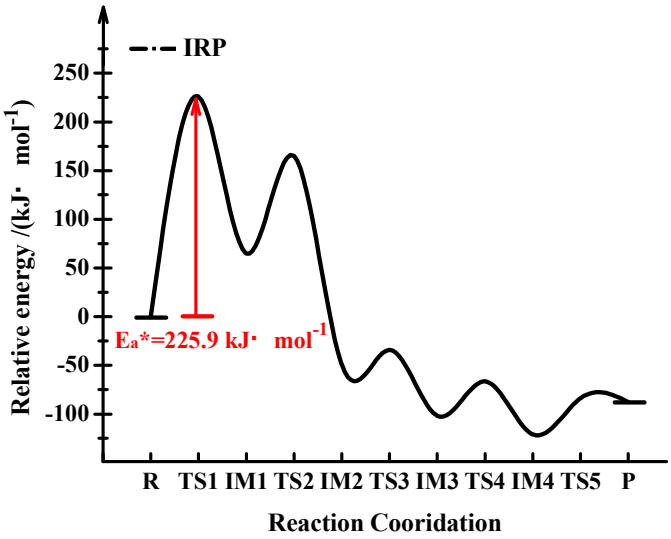

(a)

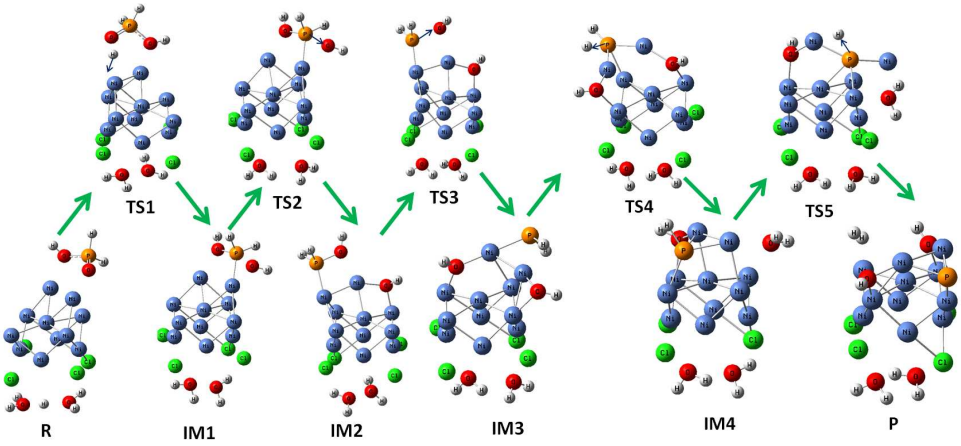

(b)

Fig. 6 Potential energy profile (a) and optimized geometries (b) for reduction of hypophosphorous acid via the IRP pathway. Energy data obtained at B3LYP/6-311G(d,p) level. (Colors: Ni-blue, O-red, P-orange, H-white; Blue arrow-direction of vibration. IM=intermediate, TS=transition state. All energies are relative to the starting materials. The blue arrows represent the vibration mode at the imaginary frequency in the transition state.)

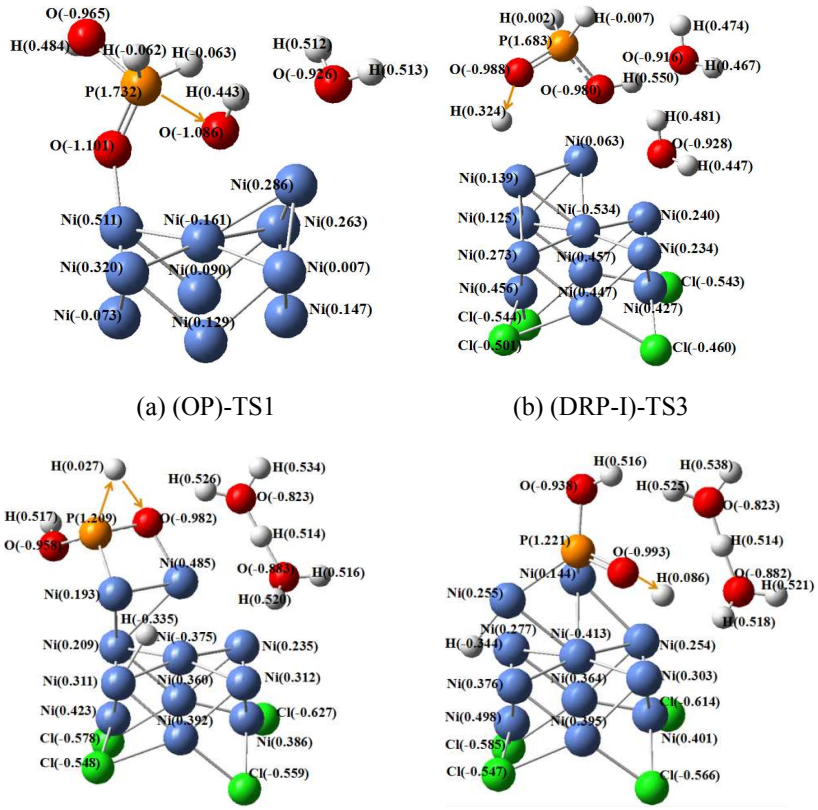

(a) (OP)-TS1 (b) (DRP-I)-TS3

(c) (DRP-II)-TS2 (d) (IRP)-TS1

Fig. 7 NBO charge distribution of TS1, TS3, TS2 and TS1 in the highest barrier site for OP, DRP-I, DRP-II and IRP pathways including Ni_9 clusters and Ni(II) ions. The data is obtained at the B3LYP/6-311G(d,p) level for main group element atoms and at the LANL2DZ level for Ni. (Colors: Ni-blue, O-red, P-orange, H-white, Cl-green; Orange arrow-direction of vibration.)

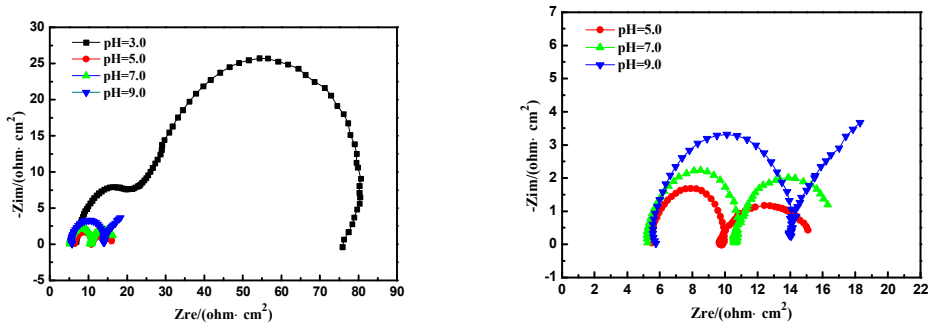

(a) (b)

Fig. 8 Nyquist impedance spectra of EN deposition in solutions with pH values of 3.0, 5.0, 7.0 and 9.0 (a), and partial spectra magnified image (b).

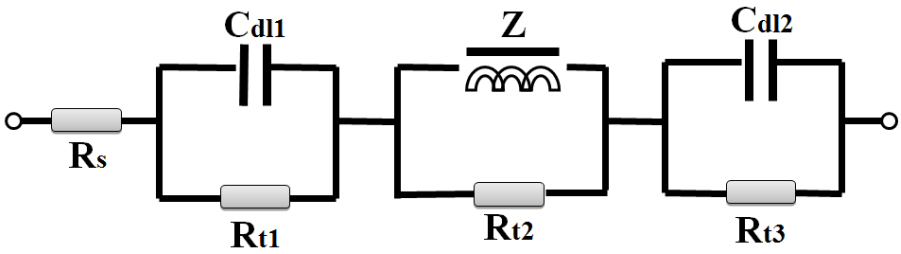

(a)

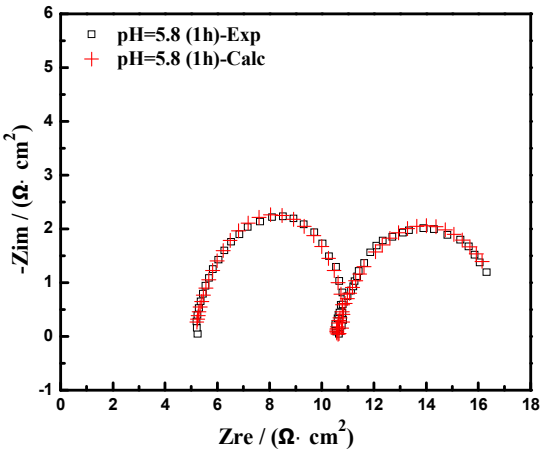

(b)

Fig. 9 An equivalent circuit model (a), and the simulated and measured impendent spectra from a solution with pH 5.8 bath in the first hour for EN process (b).

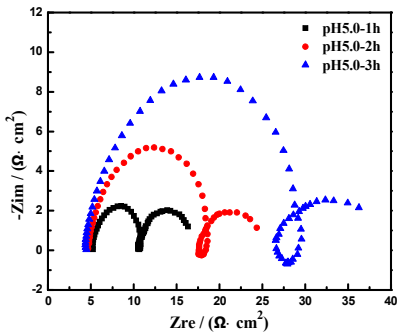

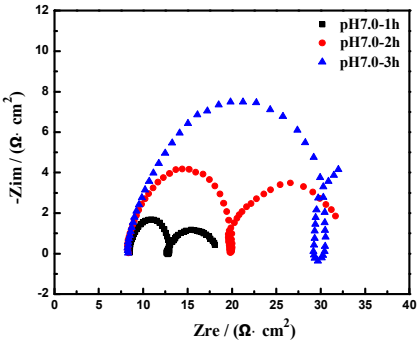

(a) (b)

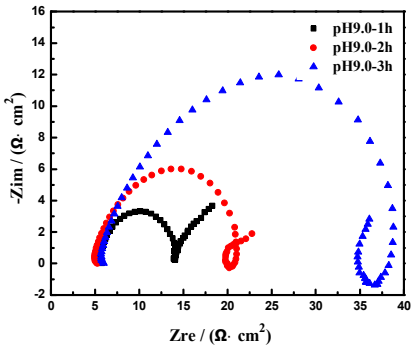

(c)

Fig. 10 Nyquist plots of electroless nickel deposition in solutions with pH values of 5.0 (a), 7.0 (b) and 9.0 (c) at different reaction times.

Table 2. Relationship of Nyqiust plot and interface reaction characteristic

Frequency domain	Electrical Element	Interfacial reaction characteristic	Related Species
High	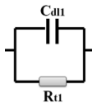	Charge-discharge in electric double layer	Ni^{2+}, $H_2PO_2^-$, $H_3PO_3^-$, H^+, OH^-
Middle	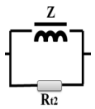	Adsorption of unstable intermediate on nickel surface	Ni(I)
Low	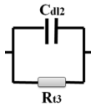	Adsorption of Ni-P compound intermediates on nickel surface	OP-IM1,H RP-IM2,IM3,IM4, P